AFRL-AFOSR-VA-TR-2022-0112

Biophysical investigations on additive manufactured nanoscale biosensors and biological materials

Priya, Shashank
PENNSYLVANIA STATE UNIVERSITY
201 OLD MAIN
UNIVERSITY PARK, PA,
US

02/16/2022
Final Technical Report

Air Force Research Laboratory
Air Force Office of Scientific Research
Arlington, Virginia 22203
Air Force Materiel Command

REPORT DOCUMENTATION PAGE

PLEASE DO NOT RETURN YOUR FORM TO THE ABOVE ORGANIZATION.

1. REPORT DATE	2. REPORT TYPE	3. DATES COVERED	
20220216	Final	START DATE 20180715	END DATE 20201214

4. TITLE AND SUBTITLE
Biophysical investigations on additive manufactured nanoscale biosensors and biological materials

5a. CONTRACT NUMBER	5b. GRANT NUMBER	5c. PROGRAM ELEMENT NUMBER
	FA9550-18-1-0233	61102F
5d. PROJECT NUMBER	**5e. TASK NUMBER**	**5f. WORK UNIT NUMBER**

6. AUTHOR(S)
Shashank Priya

7. PERFORMING ORGANIZATION NAME(S) AND ADDRESS(ES)
PENNSYLVANIA STATE UNIVERSITY
201 OLD MAIN
UNIVERSITY PARK, PA
US

8. PERFORMING ORGANIZATION REPORT NUMBER

9. SPONSORING/MONITORING AGENCY NAME(S) AND ADDRESS(ES)	10. SPONSOR/MONITOR'S ACRONYM(S)	11. SPONSOR/MONITOR'S REPORT NUMBER(S)
Air Force Office of Scientific Research 875 N. Randolph St. Room 3112 Arlington, VA 22203	AFRL/AFOSR RTB2	AFRL-AFOSR-VA-TR-2022-0112

12. DISTRIBUTION/AVAILABILITY STATEMENT
A Distribution Unlimited: PB Public Release

13. SUPPLEMENTARY NOTES

14. ABSTRACT
New tools and innovative characterization techniques must be designed to study natural materials and processes like cell signaling, neurons, nervous tissues because of limitations of present technologies. Novel in-situ characterization platform, inspired by the opto-electric interactions occurring in organohalide materials, will be developed. The platform takes advantage of the interaction of photons of well-defined wavelength and power density with biological materials. With this platform, it is possible to extract the physical properties (mobility, work function, density of states, electronic levels) by comparing the obtained data with those from complementary measurements and numerical modelling simulations. This new platform will enable us to: 1) unravel the electronic processes that occur in natural materials and living cells, representing a ground-breaking approach to investigate cellular biology, and 2) design biosensor in order to gauge how the biological material is sensitive to external stimuli such as light, temperature, magnetic fields etc. The research approach will utilize different levels of photo-stimulation and semiconductors with different energy levels and binding properties, and a combination of fully solid state and electrolytic based device platforms. Building upon the fundamental understanding of physical and electronic behavior of natural materials, novel biosensors will be fabricated using nanoprinting techniques and laser annealing.

15. SUBJECT TERMS

16. SECURITY CLASSIFICATION OF:			17. LIMITATION OF ABSTRACT	18. NUMBER OF PAGES
a. REPORT U	b. ABSTRACT U	c. THIS PAGE U	UU	24

19a. NAME OF RESPONSIBLE PERSON	19b. PHONE NUMBER *(Include area code)*
PATRICK BRADSHAW	425-8492

Title: Biophysics investigations on additive manufactured nanoscale biosensors and biological materials

Funding Agency: Air Force Office of Scientific Research (AFOSR)

Grant number: FA9550-18-1-0233

Team members:

1. Shashank Priya (PI)
   304 Old Main, Pennsylvania State University, University Park, PA
   Phone: 814-863-9657
   Email: sup103@psu.edu
2. Zhijian Pei
   Wm Michael Barnes '64 Department of Industrial & Systems Engineering
   Texas A&M University
   Emerging Technologies Building
   College Station, TX 77843-3131
   Phone: 979-458-2334
   Email: zjpei@tamu.edu
3. Thomas Brown
   Dept. Electronics Engineering
   University of Rome "Tor Vergata"
   via del Politecnico 1, 00133 Roma (Italy)
   Phone: +39 0672597779
   Email: thomas.brown@uniroma2.it

Abstract: New tools and innovative characterization techniques must be designed to study natural materials and processes like cell signaling, neurons, nervous tissues because of limitations of present technologies. Novel in-situ characterization platform, inspired by the opto-electric interactions occurring in organohalide materials, will be developed. The platform takes advantage of the interaction of photons of well-defined wavelength and power density with biological materials. With this platform, it is possible to extract the physical properties (mobility, work function, density of states, electronic levels) by comparing the obtained data with those from complementary measurements and numerical modelling simulations. This new platform will enable us to: 1) unravel the electronic processes that occur in natural materials and living cells, representing a ground-breaking approach to investigate cellular biology, and 2) design biosensor in order to gauge how the biological material is sensitive to external stimuli such as light, temperature, magnetic fields etc. The research approach will utilize different levels of photo-stimulation and semiconductors with different energy levels and binding properties, and a combination of fully solid state and electrolytic based device platforms. Building upon the fundamental understanding of physical and electronic behavior of natural materials, novel biosensors will be fabricated using nanoprinting techniques and laser annealing.

Business point of contact: Christine Woods
244 Deike Building, Penn State University, University Park, PA 16802.
Email: cnw2@psu.edu; Phone: 814-865-9786

Final Progress Report

I. Opto-electronic interactions between DNA-Perovskite Heterostructures

Deoxyribonucleic acid (DNA) has been recently recognized as hole transport material apart from its well-known generic role. The promising long-range hole transport capability in DNA makes it potential "molecular wire" in optoelectronics. Here, we demonstrated a core−shell heterostructure of perovskite wrapped by cetyltrimethylammonium chloride modified DNA (DNA-CTMA) through a self-assembly process. Such a design results in enhanced extraction and transport of holes in the bio-photovoltaic conversion and boosts the efficiency to 20.63%. The hydrophobicity of the DNA-CTMA shell surrounding the perovskite grain boundary is also found to enhance the conversion stability, as the corresponding cell retained over 90% of initial efficiency after long-term ambient exposure. Building upon the hole transport characteristics of DNA-CTMA, a hole-free conversion platform is fabricated that exhibits high power conversion efficiency but has 50,000% reduced cost. These results not only demonstrate breakthrough in designing cheap, efficient, and stable biophotovoltaics but also open the pathway towards the exciting possibility of controlled interaction between living and artificial semiconductors.

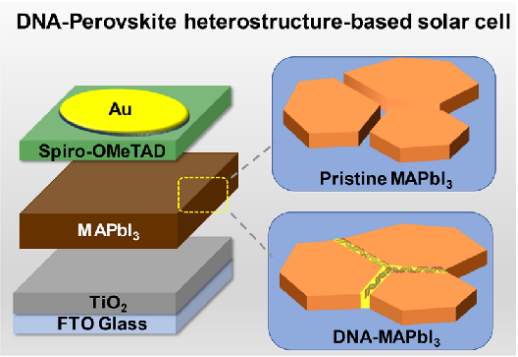

Figure 1: Schematic description of DNA architecture in organohalide microstructure.

Results: Deoxyribonucleic acid (DNA) carries genetic information in nearly all living organisms. Study on DNA in the past decade has shown that this material can also exhibit promising electronic transport. The charge diffusion length of over 100 nm has been observed in single DNA strand. DNA molecule has been shown to exhibit a coherent long-range hole transport along the chain length due to the strong delocalized highest occupied molecular orbitals (HOMOs) of G nucleobase. These prior results provide opportunity towards developing bioelectronic platforms with DNA as the functional component. DNA thin films have been employed as building blocks in nanomachines and charge extraction or blocking interlayer in solid-state devices such as organic light-emitting diodes (OLEDs) and organic field-effect transistors (OFETs). Here, we demonstrated DNA – $CH_3NH_3PbI_3$ ($MAPbI_3$) composites for high efficiency perovskite solar cells (PSCs). A self-assembly process was developed to synthesize a core-shell heterostructure where modified DNA-CTMA molecules occupy the perovskite grain boundaries. This heterostructure architecture allows the hole carriers to be effectively extracted from perovskite and then transferred to hole transport layer (HTL). Additionally, the trap sites at grain boundaries are passivated through bonding between DNA molecules and perovskite, thereby, reducing the non-radiative recombination loss. As a result, the PSC devices based on bio-perovskite hybrid composite attained high power conversion efficiency (PCE) of 20.63%. The HTL-free PSC devices attained a PCE of 14.05%, which is nearly 65% higher compared with pristine device. In addition, the incorporation of DNA-CTMA molecule on grain boundaries of perovskite film reduced the degradation against environmental stimuli; increasing device stability for long-term operation.

To better understand the chemical bonding between $MAPbI_3$ perovskite and DNA-CTMA strands, a model is presented to illustrate the interaction between DNA biomolecule and $MAPbI_3$

crystal, as shown in Fig. 2. In this model, CTMA side chains were assumed to have little interaction with $MAPbI_3$ and are thus not included. Interestingly, the spacing of the lead atoms (Pb) exposed on the perovskite lattice surface perfectly matches the inter-phosphate (PO_4) distances along the minor and major grooves in the DNA, which are both ~6.2 Å, resulting in strong electrostatic bonds along the perovskite/DNA interface. Lead and phosphate group are known to form strong electrostatic interactions as seen in many lead phosphate crystal structures. In DNA molecular structure, the anionic phosphinyl portion of phosphate groups are Lewis bases which can interact with Lewis acids and the lead ions in $MAPbI_3$, to form an electrostatic bond between DNA and $MAPbI_3$ perovskite. To verify this model, electron energy loss spectroscopy (EELS) was conducted to analyze the electronic state of Pb atom in perovskite. The electron beam is focused on the interface between DNA and $MAPbI_3$. In comparison with pristine $MAPbI_3$ perovskite, the Pb M2 and M3 edges are obviously shifted upon integration of DNA molecules. The energy shift originates from the Pb-PO_4 interaction that changes coordination environment of lead atom in $MAPbI_3$[32]. The established strong electrostatic bonding between lead in $MAPbI_3$ and phosphate groups in DNA not only drives the formation of DNA-$MAPbI_3$ heterostructure but also enables the efficient hole -transfer from $MAPbI_3$ perovskite into the DNA backbone.

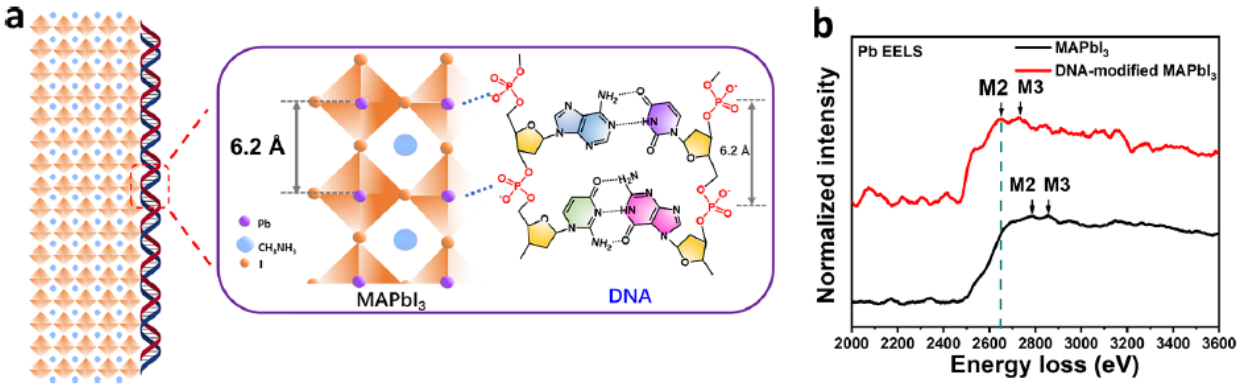

Figure 2: Bonding interaction between DNA and perovskite. (a) A molecular model showing a possible mode of DNA binding with the MAPbI3 lattice, which implies that the spacing of the lead atoms (Pb marked in purple) in the MAPbI3 lattice matches the inter phosphate (PO4 group marked in red) distances (~6.2 Å) in DNA resulting in strong electrostatic bonds at the perovskite/DNA interface. (b) EELS plot showing the shift of Pb M2 and M3 edge in DNA-modified MAPbI3 compared with pristine sample.

This was an early study on the incorporation of DNA within the organic-metal halide perovskite $MAPbI_3$. Results clearly depicted the formation of nanoscopic structure of DNA-CTMA molecules coupled with perovskite crystals, where DNA molecules are assembled around perovskite grains forming a core/shell heterostructure. The shell layer of hole-conducting DNA-CTMA molecules around the perovskite grains facilitated hole transfer and transport. Electronic properties of the $MAPbI_3$ films were characterized by Kelvin probe force microscopy (KPFM). The contact potential difference (CPD) images of pristine and DNA-modified $MAPbI_3$ film were analyzed to quantify the magnitude of band levels. CPD reflects the potential difference between work function of tip (Φ_{tip}) with respect to sample (Φ_{sample}), which can be used to estimate the Fermi level of perovskite film. Fermi level of pristine and DNA-modified perovskite film was determined to be -4.907 eV and -5.013 eV, respectively. The Fermi level of perovskite film is decreased after DNA incorporation, suggesting a more p-type characteristic. The change of carrier concentration in

$MAPbI_3$ upon DNA modification was studied by measuring the capacitance response of device under applied voltage ($1/C^2$-V curve) in the dark. Carrier concentration can be extracted from $1/C^2$-V curve by Mott-Schottky analysis. The hole concertation in the pristine $MAPbI_3$ is calculated to be 3.65 x 10^{15} cm^{-3}, which increases to 7.38 x 10^{15} cm^{-3} after DNA incorporation, thus exhibiting a more p-type characteristics.

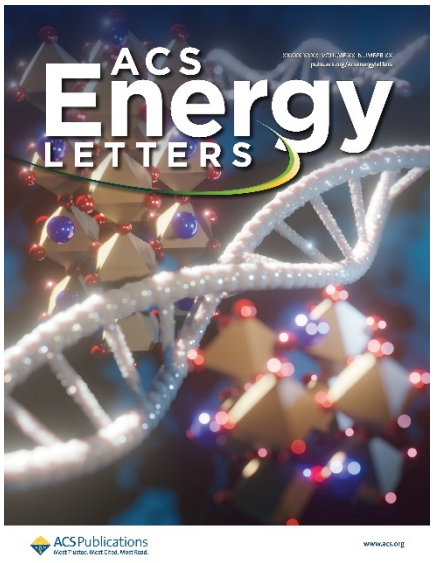

In future, we would like to build upon this study and conduct comparative analysis of the control samples with the DNA-modified samples. This will allow us to quantify the electrical properties of the DNA as a function of sequences and various modifications. We believe these results will have transformative impact on the design and development of biosensors.

II. Bacteriorhodopsin Enhances Efficiency of Perovskite Solar Cells

Summary - Recently, halide perovskites have shown promising opto-electrical conversion by reaching power conversion efficiencies that surpass the performance of polycrystalline silicon. The efficiency improvement in the perovskite cells is related to repeated recycling between photons and electron−hole pairs, reduced recombination losses, and increased carrier lifetimes. Here, we demonstrate a novel approach toward augmenting the perovskite solar cell efficiency by invoking the Förster Resonance Energy Transfer (FRET) mechanism. FRET occurs in the near-field region as the bacteriorhodopsin (bR) protein, and perovskite has similar optical gaps. Titanium dioxide functionalized with the bR protein is shown to accelerate the electron injection from excitons produced in the perovskite layer. FRET predicts the strength of long-range excitonic transport between the perovskite and bR layers. Solar cells incorporating TiO2/bR layers are found to exhibit much higher photovoltaic performance as compared to baseline cells without bR (Figure 3). These results open the opportunity to develop a new class of bioperovskite solar cells with improved performance and stability.

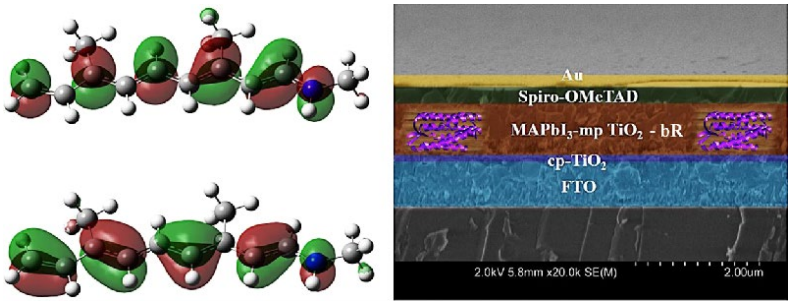

Figure 3: Summary schematic showing the bR protein structure and the multilayer platform for studying its effect in opto-electric conversion.

Results – We developed a new type of bio-perovskite solar cell (BPSC), as illustrated in Figure 4. The band alignment is illustrated in Figure 4a, and the schematic architecture of the BPSC is displayed in Figure 4b. The valence band edge of CH3NH3PbI3 (MAPbI3) is located at −5.3 eV, which is lower than the highest occupied molecular orbital (HOMO) of Spiro-OMeTAD hole-

transport layer, HTL (−5.2 eV). The conduction band edge of MAPbI3 is at −3.7 eV, which is higher than that of the TiO2 electron transport layer, ETL (−4.2 eV). The favorable band alignment of perovskite with the TiO2 ETL and Spiro-OMeTAD HTL allows the extracted charge carriers to be transported to electrodes. The key components of the BPSC are the bR molecules between TiO2 and perovskite layers, which implement the energy transfer step involving photon absorption and hot carrier transfer. The light energy conversion is realized through the transfer of photogenerated electrons from the perovskite absorber to bR molecules through the Förster resonance energy transfer (FRET) process. The photogenerated electrons are subsequently transferred to TiO2 driven by the difference in energy level between bR and TiO2. The bR bridging perovskite and TiO2 are found to assist the electron transfer and significantly reduce the interfacial charge recombination, which led to improved power conversion efficiency. This novel BPSC architecture utilizes the natural biomaterials for light energy conversion, thereby providing the environmentally friendly structure for design of efficient solid-state photovoltaic devices.

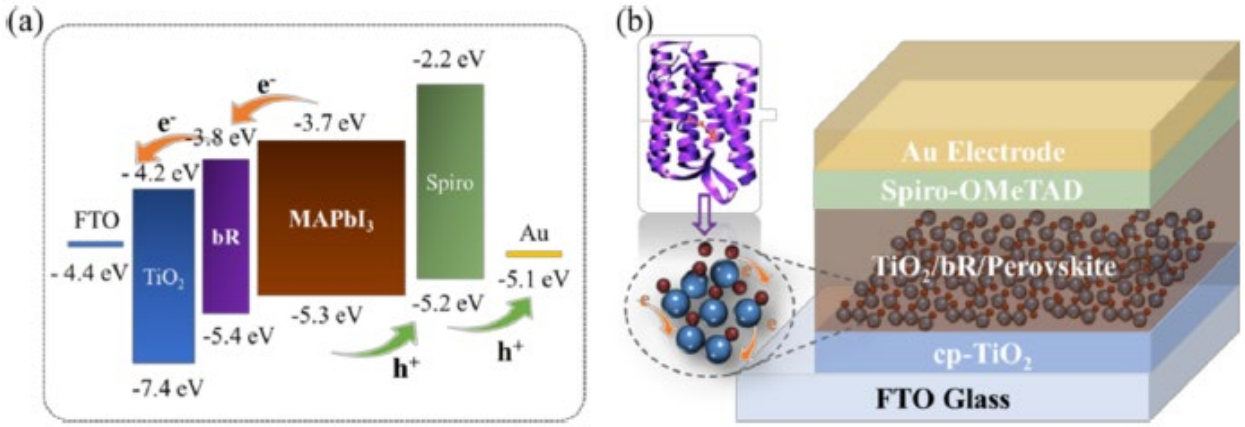

Figure 4. (a) Band alignment of the BPSC. (b) Schematic of the BPSC architecture, where the compact TiO2 layer, perovskite/mesoporous TiO2/bR, Spiro-OMeTAD, and Au electrode were deposited on FTO glass, respectively.

III. Melanin–Perovskite Composites – Photothermal Conversion Phenomenon

Biomacromolecular pigments, such as melanin, play an essential role in the survival of all living beings. Melanin absorbs sunlight and transforms it into heat, which is crucial for avoiding damage to skin cells. Light absorption produces excited electrons, which could either fall back to ground states by releasing the heat (photothermal effect) and/or light (photoluminescence), or stay at higher energy levels within its lifetime period, which can be captured through external electronic circuitry (photovoltaic effect). We demonstrated that the combination of melanin with halide perovskite light absorber in the form of a composite exhibits high absorbance from the UV to NIR region in the solar spectrum. And the composite displays significantly reduced photoluminescence and minimized density of residual excited states (verified by photovoltaic measurement) owing to the significantly enhanced nonradiant quenching by the melanin. As a result, the composite shows an ultrahigh solar-thermal quantum yield of 99.56% and solar-thermal conversion efficiency of ≈81% under one-sun illumination (AM1.5), which is superior to typical carbon materials such as graphene (≈70%). By coating the photothermal composite film on the hot-side of thermoelectric devices, a 7000% increase in output power as compared to the blank device under illumination is observed.

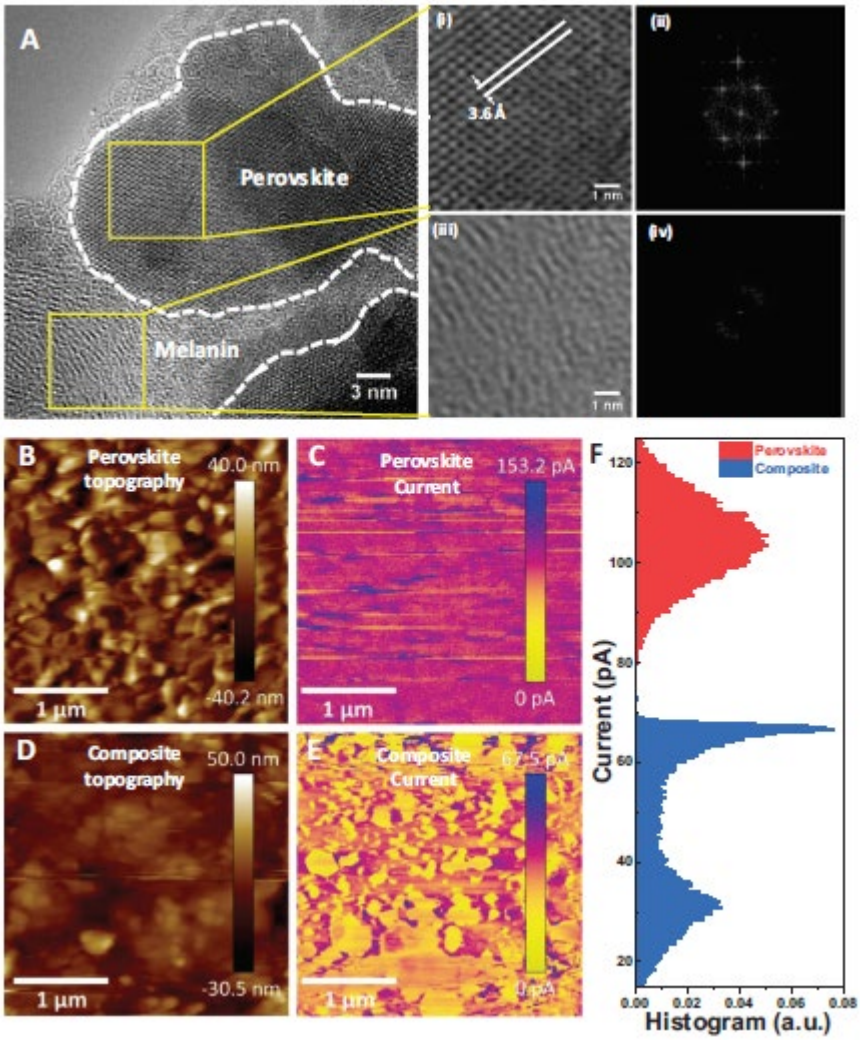

Figure 5. *Distribution of melanin in perovskite. A) HRTEM images of a melanin–perovskite composite sample, where the edges of the perovskite crystallites are denoted by white dot line. Yellow square denotes either (i) perovskite domain with its corresponding (ii) FFT image, or the (iii) melanin domain with its corresponding (iv) FFT image. B–E) CAFM measurements on pristine–perovskite and the composite samples. Topographical images of B) pristine perovskite and D) the melanin–perovskite composite; the corresponding current map of C) perovskite and E) composite under a sample bias of 1 V. F) Current histogram of perovskite and composite corresponding to the current in (C) and (E), respectively.*

To visualize the microstructural feature of the composite and the distribution of the melanin in the composite, we employed the high-resolution transmission electron microscopy (HRTEM) to investigate the melanin–perovskite composite. **Figure 5**A shows the HRTEM image of the composite sample, where the amorphous melanin is well distributed between the crystallites. We measured the *d*-spacing to be 3.6 Å (Figure 5Ai), which is consistent to the {022} planes of MAPbI3 perovskite (space group of *I*4/*mcm*). And the corresponding fast Fourier transform (FFT) (Figure 5Aii) exhibits a clear scattering pattern, representing the well-defined perovskite crystals. In contrast, the melanin between the perovskite crystallites shows the typical amorphous morphology (Figure 5Aiii) and there is no scattering pattern in the corresponding FFT image

(Figure 5Aiv) but amorphous halo which is consistent to typical amorphous nature of melanin macromolecules. Hence, the melanin is confirmed to be distributed at the grain boundaries between the perovskite crystallites. To further understand their microscopic distribution, we employed the conductive atomic force microscopy (CAFM) to visualize the surface current map of the composite. The perovskite is more electrically conductive with an electrical conductivity of (10^{-2} S cm^{-1}) than the melanin (10^{-6} S cm^{-1}). Thus, the more insulating melanin-rich phase in the matrix can be distinguished from the current map. Figure 5B–E shows the topography and current images of pristine perovskite and the melanin–perovskite composite. The pristine–perovskite sample exhibits a generally more homogeneous current image with an average current of =104 pA (Figure 5C). While the composite sample exhibits regions with different current intensities and an overall lower current value (Figure 5E). Figure 5F quantifies their current histograms. In contrast to the unimodal current distribution in pristine–perovskite, the composite exhibits a multimodal distribution, where the higher-current peak is corresponding to the more electrically conductive perovskite rich region and the lower-current peak is corresponding to the melanin-rich region, which is more electrically insulating. Thus, the melanin is concluded to be distributed between the perovskite crystallites at a scale from nanometer to sub-micrometer.

The incorporation of melanin significantly reduces the radiant recombination of perovskite by supplying drastic recombination centers for nonradiant relaxation. Hence, the photogenerated excited electrons are easily de-excited to the ground states by means of SRH recombination, releasing the heat. PL study confirms that the significantly reduced radiant recombination and the corresponding solar cell evaluation show the significant recombination loss of the photoexcited charge carriers. Microscopic characterizations suggest that the melanin can be distributed between the perovskite crystallites forming a monoscopically phase-separated composite. By continuous solar radiation, the melanin–perovskite composite exhibit efficient solar thermal conversion with a high solar thermal conversion efficiency of 81% under one-sun illumination (AM1.5), higher than typical inorganic materials such as plasmonic nanoparticles and metal oxide nanoparticles. This study opens a new window of a photothermal application by means of mixing halide perovskite with biologic pigment.

IV. Three-dimensional printing of functional materials

We developed design and manufacturing routes to demonstrate previously inaccessible classes of piezoelectric materials that have arbitrary piezoelectric coefficient tensors. Our scheme is based on the manipulation of electric displacement maps from families of structural cell patterns. We implement our designs by additively manufacturing free-form, perovskite-based piezoelectric nanocomposites with complex three-dimensional architectures. The resulting voltage response of the activated piezoelectric metamaterials at a given mode can be selectively suppressed, reversed or enhanced with applied stress. Additionally, these electromechanical metamaterials achieve high specific piezoelectric constants and tailorable flexibility using only a fraction of their parent materials. This strategy may be applied to create the next generation of intelligent infrastructure, able to perform a variety of structural and functional tasks, including simultaneous impact absorption and monitoring, three-dimensional pressure mapping and directionality detection. To implement this concept, we prepared functionalized lead zirconate titanate (PZT) nanoparticle colloids. These nanoparticles are then covalently bonded with entrapped photo-active monomers. These concentrated piezoelectric colloids are subsequently sculpted into arbitrary 3D form factors through high-resolution additive manufacturing. We found that building blocks with designed

piezoelectric signatures could be assembled into intelligent infrastructures to achieve a variety of functions, including force magnitude and directionality sensing, impact absorption and self-monitoring, and location mapping, without any additional sensing component. These free-form PZT nanocomposite piezoelectric metamaterials not only achieve a high piezoelectric charge constant and voltage constant at low volume fractions but also simultaneously possess high flexibility, characteristics that have not been attainable in previous piezoelectric foams or polymers.

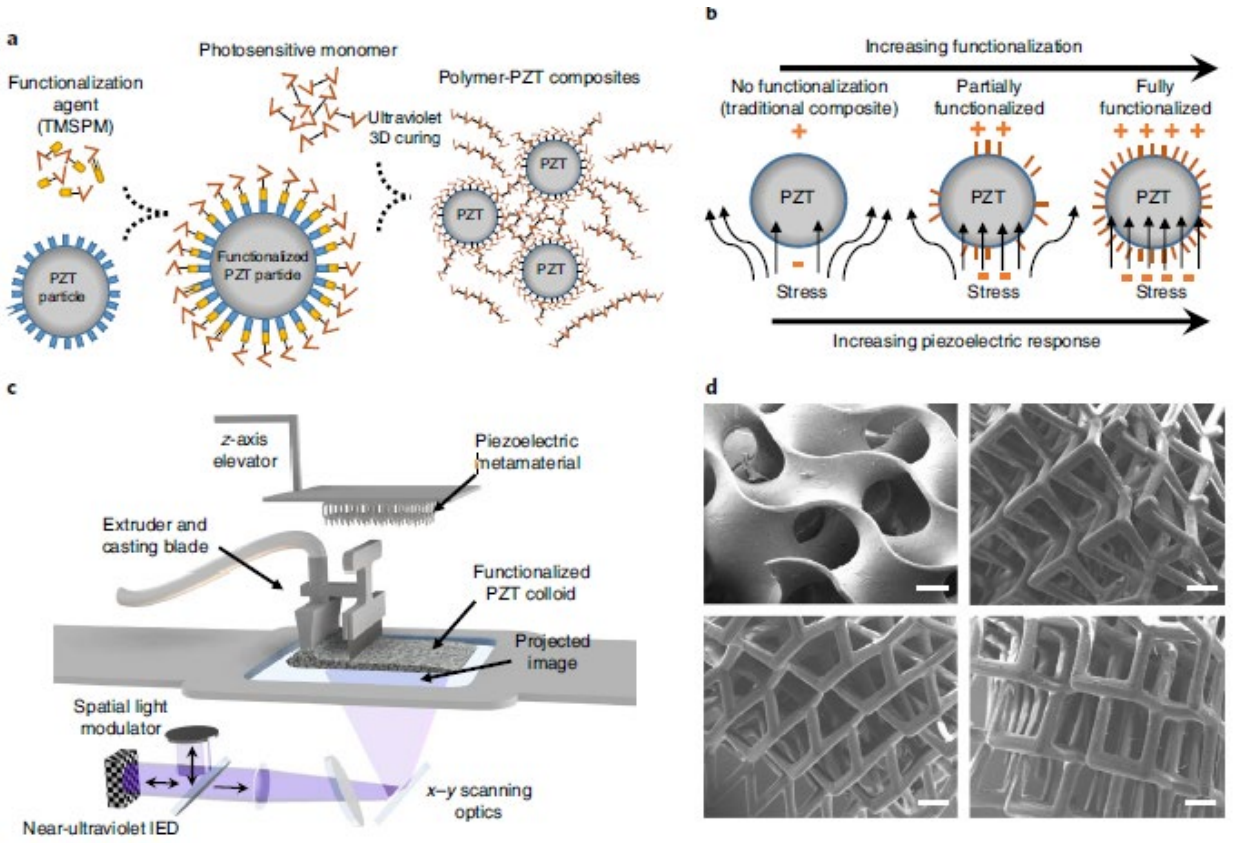

Figure 6. *Surface functionalization of PZT with photosensitive monomers and 3D printing of piezoelectric metamaterials with complex microarchitectures.* ***a****, Schematic illustration of surface functionalization method and strong bonds between the nanoparticles and the polymer matrix after the ultraviolet curing process.* ***b****, Schematic illustration of the relationship between the surface functionalization level and the piezoelectric response. The piezoelectric response increases with the surface functionalization level as a result of increasing stress transfer.* ***c****, Schematic illustration of the high resolution additive manufacturing system.* ***d****, Scanning electron microscope images of 3D-printed piezoelectric microlattices. Scale bars, 300 μm.*

Our fabrication method of 3D piezoelectric architectures starts by synthesizing surface-functionalized piezoelectric nanoparticles (Fig. 6a,b), dispersing them with ultraviolet-sensitive monomers into highly concentrated, uniform colloids (PZT volume loading up to 50%) that can be sculpted into 3D structures by near-ultraviolet light (Fig. 6c). While surface functionalization of approximately 4 vol% piezoelectric nanoparticles has produced an appreciable piezoelectric coefficient as compared to non-functionalized dispersion, the trade-off between high piezoelectric responsiveness and processability has limited the realizations of arbitrary piezoelectric 3D micro-

architectures with high piezoelectric coefficients. As shown in Fig. 6a, a functionalization agent, (trimethoxysilyl propyl methacrylate) is covalently grafted to the PZT particle surface via siloxide bonds leaving free methacrylate on the surface. The surface functionalization reaction is optimized to maximize surface coverage. These strong covalent bonds between the piezoelectric nanoparticles and the polymer matrix network improve the dispersion quality of the highly concentrated piezo-active colloidal resin by creating a sterically hindered surface. Increasing the functionalization level elevates the piezoelectric output of the nanocomposite to reach the upper bound at a given loading concentration (Fig. 6b). Strict control of the thickness of the colloidal paste through the designed recoating system and reduction of oxygen inhibition enable the fabrication of complex 3D piezo-active architectures with fine features from a range of concentrated colloidal particles entrapped with ultraviolet-sensitive monomers (Fig. 6c–d). This versatile process is not limited to PZT. Surface functionalization can be implemented to enhance the response of a wide range of piezoelectrics (for example, barium titanate, BTO) or other functional materials such as multiferroics (for example, bismuth ferrite). The as-fabricated nanocomposite system does not require post-heat treatment, and achieves high structural fidelity and uniformity. Configuring the photo-sensitive monomer compositions enables independent tuning of the composite stiffness, allowing us to access rigid to flexible piezo-active materials to convert mechanical stress to voltage signals.

V. 3D Printing of Hydrogel Filters Containing Algae Cells for Copper Removal from Contaminated Water

Note: The results from this study will be published in a journal paper:
Thakare, K., Jerpseth, L., Pei, Z.J., Tomlin, B., and Qin, H.M., 2021, "3D printing of hydrogel filters containing algae cells for copper removal from contaminated water," accepted to appear in Journal of Manufacturing Science and Engineering.

Introduction

Copper in contaminated water can have detrimental impacts to human health. Copper toxicity caused by contaminated water cannot be processed by the liver, and accumulates in the blood [1]. Copper toxicity is correlated with cognitive decline [2], lysis of blood cells, and liver scarring [3]. Chronic copper toxicity can cause coma, blood vessel collapse, and death [4]. It is estimated that the tap water in about 30% of American households is contaminated with copper, putting millions of Americans at risk of copper poisoning [1]. In the year of 2006, Cech et al. tested the water of 45 drinking fountains in five public buildings in Houston, Texas [5]. They found that the copper concentration was up to 5 ppm [5], exceeding the maximum allowable level of 1.3 ppm set by the Environmental Protection Agency (EPA) [6]. In addition, copper contamination can also be harmful to the environment. It was reported that copper concentration in 86% of San Diego's marine areas exceeded EPA's allowable level [7]. Copper contamination can cause abnormal embryo development in marine animals [7], and negatively affect gills, liver, and intestines of fish [8].

Reported approaches to removing heavy metals (including copper) from contaminated water include chemical approaches (such as chemical precipitation [9-11] and carbon adsorption [12-14]) and physical approaches (such as reverse osmosis [15-17]). These approaches can be expensive, because removal of metal ions from aqueous solution is not thermodynamically efficient with current approaches [18]. Additionally, the use of chemicals may lead to secondary

contamination, i.e., the chemicals used in water treatment may themselves contaminate the water [19, 20].

Besides, there are biological approaches. One of them is to use algae suspended in water. This approach is more accessible in places without complex infrastructure [19]. After water treatment, the algae can be used as feedstock materials for production of biofuel and fertilizer [21]. Currently, however, suspended algae are not used to treat contaminated water at an industrial scale due to a number of technical barriers. It is difficult and expensive to collect algae after treatment [19, 21]. Chemical agents are often used to harvest suspended algae from water, creating chemical waste [22]. Furthermore, suspended algae that are not removed from natural bodies of water might lead to algae blooms, i.e. excessive growth of algae [19, 23]. Algae blooms can have several detrimental impacts; for example, depleting oxygen in marine bodies as algae decompose [24]. The depletion of oxygen can kill marine life and decrease biodiversity [25].

Printed hydrogel filters containing algae cells can potentially overcome these technical barriers. After treatment of contaminated water, these hydrogel filters containing algae cells can be easily removed from water without using chemical agents. Furthermore, because algae cells are immobilized in the hydrogels of printed filters, there is very limited chance for the algae to leak out, contaminate treated water, or cause algae blooms in natural bodies of water.

Currently, the literature has no reported study on 3D printing of hydrogel filters containing algae cells for copper removal from contaminated water. This paper reports the first study in the literature on 3D printing of hydrogel filters containing algae cells for copper removal from contaminated water. In this study, hydrogel filters containing algae cells and those containing no algae cells were printed on an extrusion-based 3D printer. They were then used in a custom-build filtration setup for copper removal. Test solution with copper concentration of 3 ppm was prepared and circulated through the filtration system for 4 hours. Samples of the test solution were taken every one hour. Copper concentration data of these samples were analyzed.

Materials and Methods

Preparation of algae cells

A 150-milliliter flask (VWR, USA) was used to prepare 100 milliliters of tris-acetate-phosphate (TAP) culture media. *Chlamydomonas reinhardtii* algae strain cc125 cells were streaked off from a petri dish and added to the flask. The addition was done in a biosafety cabinet (SterilGARD III Advance, Baker, USA) to maintain a sterile condition. The *Chlamydomonas reinhardtii* algae strain cc125 was selected because it is commonly used in laboratories. The algae cells used in this study were obtained from the *Chlamydomonas* Center (Chlamydomonas Resource Center, University of Minnesota). The flask (containing the TAP-algae solution) was put on a shaker (New Brunswick Scientific Co., Inc, USA) for 72 hours. The shaker was run at 100 rpm and kept at 22 °C, under lightbulbs to allow growth of the algae cells. Afterwards, the algae cell quantity in the TAP-algae solution was measured using Auto T4 cell counter (Nexcelom, USA) according to the instructions from the cell counter manufacturer. The new flask of the TAP-algae solution was then placed under lightbulbs for 24 hours to allow algae cells to grow.

Preparation of hydrogel bioink

The bioink was based on alginate:methylcellulose hydrogel. Alginate is a natural polymer derived from algae, and methylcellulose is a polymer consisting of numerous linked glucose molecules. Three grams of alginic acid sodium salt (Sigma-Aldrich, USA) were added to 100 milliliters of deionized water in a 500-milliliter beaker (VWR, USA). This alginate solution was

stirred at 900 rpm for five hours on a hot plate stirrer (Fisher Scientific, USA). The alginate solution was then heated on the hot plate stirrer to 90°C, and six grams of methylcellulose powder (Sigma-Aldrich, USA) were added to the solution. The alginate:methylcellulose solution was autoclaved in an autoclave (LG 250 Sterilizer, Steris, USA) for one minute at 121°C to achieve sterilization. The time and temperature settings for autoclaving were chosen to ensure sterility of the alginate:methylcellulose solution without burning the methylcellulose. After the alginate:methylcellulose solution cooled to room temperature, algae cells in the TAP-algae solution were added to the alginate:methylcellulose solution. The addition of algae cells was performed by pipette (Rainin, USA), an instrument used to deposit precise volumes. The addition was done in a biosafety cabinet (SterilGARD III Advance, Baker, USA). The algae cell concentration in the bioink was 150,000 cells per milliliter of bioink.

Design and printing of hydrogel filters

The filter was designed using Fusion 360 (Autodesk, USA). The filters had a shape of a square disk. Its length was 25 millimeters and thickness was 1.5 millimeters. It also had 8 through holes with a diameter of 2 millimeters. The STL file generated by Fusion 360 software was converted into a G-code file using SLICER software (SLICER.org, USA). This G-code file was then imported into Allevi bioprinter software (Allevi Inc, USA).

Allevi 1 bioprinter (Allevi Inc, USA) was used to print the filters. Five milliliters of bioink were loaded into the extrusion syringe (Allevi Inc, USA) equipped with a 30-gauge needle (Allevi Inc, USA). Each of the filters was printed on a 10-centimeter petri dish (VWR, USA). Printing speed was 6 millimeters/second and extrusion pressure was 95 psi. The layer height was 0.1 millimeters.

Immediately after printing, 5 milliliters of 4% w/v $CaCl_2$ solution was added to the petri dish containing the printed filter for two minutes to allow for crosslinking of alginate [36]. After crosslinking was completed, liquid TAP media was then poured over the filters to allow the algae cells to grow. The filters were then kept at room temperature, under lightbulbs for four days to give the algae cells sufficient time to grow.

Hydrogel filters containing algae cells and those containing no algae cells were printed using the same printing conditions and on the same day.

Custom-made filtration setup

The custom-made filtration setup was fabricated which consisted of a peristaltic pump, pump tubing, a filtration chamber, an outflow tube, a valve, and a beaker. The filtration chamber consisted of a segment of acrylic cylinder, and four platforms printed using Stratasys PolyJet 750. The circular platforms had a diameter of 46 millimeters, and a total height of 22 millimeters. The platforms were vertically stackable, allowing them to be placed on top of each other. Each platform had a recess with a sieve-like bottom (for placing a printed filter). The sieve-like bottom had 13 holes with a diameter of 2 millimeters. The bottom end of the filtration chamber was connected to a valve to control the flow rate of test solution going out of the chamber. An outflow tube was connected to the valve at one end (with the other end inside a beaker), to direct the flow of test solution out from the filtration chamber. A 100-milliliter beaker (VWR, USA) was used to collect the test solution from the outflow tube. The peristaltic pump (Model no. 3386, Control Company, USA), together with pump tubing, was used to circulate the test solution from the beaker through the filtration chamber. One end of the pump tubing was placed inside the beaker and the other end was placed inside the filtration chamber.

Test solution preparation

The following steps describe the test solution preparation.

Step 1: A 500-milliliter beaker (VWR, USA) was filled with 200 milliliters of ultrapure 18.2 megohm water. The ultrapure water was obtained from an Ultrapure water filtration system (Barnstead, USA), and contains less than 0.00001 ppm of trace metals.

Step 2: Using a pipette (Rainin, USA), 0.6 milliliters of ultrapure water were removed from the beaker, leaving 199.4 milliliters of water inside the beaker.

Step 3: Using a pipette, 0.6 milliliters of 1,000 ppm copper stock solution (Sigma-Aldrich, USA) were added to the beaker of ultrapure water. The copper concentration of the 200 milliliters of test solution in the beaker became 3 ppm.

Step 4: The test solution was evenly divided, with the help of a pipette, into two separate 250-milliliter beakers, each containing 100 milliliters of test solution.

The test solution in one beaker was for the filtration experiment using hydrogel filters containing algae cells, and the test solution in the other beaker was for the filtration experiment using hydrogel filters containing no algae cells. The test solution was prepared on the same day the filtration experiments were performed. Copper concentration of 3 ppm was chosen to compare with a previously published study.

Filtration experiment procedure

The filtration experiment setup was put together and the filtration experiments were performed in the biosafety cabinet to prevent contamination. The filtration experiment procedure had the following steps.

Step 1: The components of the filtration setup were placed inside the biosafety cabinet.

Step 2: A hydrogel filter was placed on one of the 3D printed platforms.

Step 3: The platform, together with the filter, was placed inside the filtration chamber.

Step 4: Step 2 and step 3 were repeated until all four platforms (and hydrogel filters) were vertically stacked inside the filtration chamber.

Step 5: The valve at the bottom of the filtration chamber was closed, and 100 milliliters of test solution was pumped into the chamber from the 250-milliliter beaker. This amount of test solution in the filtration chamber was enough to completely submerge the platforms and filters.

Step 6: The valve was opened to allow the test solution to flow out of the filtration chamber through the outflow tube and into the beaker. The valve was set to allow a flow rate of 15 milliliters/minute.

Step 7: After the valve was opened, the peristaltic pump was set to continuously pump the test solution from the beaker into the filtration chamber. The flow rate of the pump was also set at 15 milliliters/minute. This was done to maintain constant volume of test solution in the chamber. Approximately 5 milliliters of test solution were in the beaker at any time, and 95 milliliters of test solution were in the filtration chamber.

The same filtration procedure was followed for the experiment using hydrogel filters containing algae and those without algae. Both experiments were conducted on the same day.

Sample collection and measurement of copper concentration of the samples using ICP-MS

The filtration experiment started when the valve was opened, and ended after 4 hours. Three samples of test solution were taken from the beaker at the start of the experiment and at intervals of 1 hour, until 4 hours had passed.

The following steps are for collecting samples, preparation of the samples for copper concentration measurement, and copper concentration measurement on the inductively coupled plasma-mass spectrometry (ICP-MS).

Step 1: For each sample, approximately 0.2 milliliters of test solution was collected and put in a 1.5-milliliter Eppendorf tube (Eppendorf, USA).

Step 2: For each sample, there was a 50-milliliter BD tube (Becton Dickinson, USA) filled with 10 milliliters of 2% nitric acid. The 2% nitric acid was prepared by diluting 70% TraceMetal Grade nitric acid (Fisher Scientific, USA) with ultrapure 18.2 megohm water.

Step 3: The test solution samples were diluted. To perform the dilution, a pipette was used to transfer 0.01 milliliters of test solution from the Eppendorf tube to a BD tube containing 10 milliliters of 2% nitric acid. It was necessary to dilute the samples by a factor of 1,000, because the ICP-MS instrument cannot measure copper concentration above 0.2 ppm.

Step 4: ICP-MS was used to measure the copper concentrations of the diluted samples in the BD tubes. Prior to every measurement, a solution of 2% nitric acid was used to wash off residual copper left on the instrument from the previous measurement.

Results and Discussion

For the hydrogel filters containing algae cells, between the start of the filtration experiment and 1 hour filtration time, copper concentration decreases by 82.3%. After 2 hours of filtration, copper concentration decreases to below the detection limit of the ICP-MS instrument. Conservatively, this detection limit is 0.001 ppm [38]. Copper concentration remains below the detection limit of the ICP-MS instrument for filtration time of 3 hours and 4 hours. Observing the relationship curve for the hydrogel filters containing no algae cells, between the start of the filtration and 1 hour filtration time, copper concentration decreases by 47.8%. By 2 hours of filtration time, copper concentration decreases by 82.5% from the initial copper concentration. This decrease in copper concentration is relatively smaller in comparison to hydrogel filters containing algae cells. Copper concentration of test solution filtered by hydrogel filters containing no algae cells decreases below the ICP-MS detection limit at 3 hours of filtration time and remains below the detection limit at 4 hour filtration time. The hydrogel filters containing algae cells can remove copper almost twice as fast as hydrogel filters containing no algae cells.

Non-parametric Kruskal-Wallis tests were conducted to evaluate whether there is a statistically significant relationship between copper concentration of test solution and filtration time (ANOVA analysis could not be used for this purpose because the two basic assumptions were not met). A p-value of 0.0082 was obtained on performing the Kruskal-Wallis tests. This indicates that, at the significance level of 0.01, there is a statistically significant relationship between copper concentration and filtration time.

In a study conducted by the authors, suspended algae cells were used to remove copper from test solutions [37]. Two levels of initial copper concentration of the test solutions were 1.5 and 3 ppm, respectively. Two levels of contact time (of algae with test solutions) were 2.5 and 5 hours, respectively. Four possible combinations of initial copper concentration and contact time were tested. The suspended algae were able to decrease copper concentration from 1.5 ppm to 0.038 ppm after 2.5 hours. For comparison, printed algae filters were able to decrease copper concentration from 3 ppm to less than 0.001 ppm after two hours.

It was concluded that hydrogel filters with and without algae cells can reduce copper concentration in test solution, and hydrogel filters containing algae cells remove copper twice as fast as hydrogel filters containing no algae cells.

VI. Bioprinting Using Algae: Effects of Extrusion Pressure and Needle Diameter on Cell Quantity in Printed Samples

Note: The results from this study have been published in a journal paper:
Thakare, K., Jerpseth, L., Qin, H.M., and Pei, Z.J., 2021, "Bioprinting using algae: effects of extrusion pressure and needle diameter on cell quantity in printed samples," Journal of Manufacturing Science and Engineering, Vol. 143, No. 1, 014501. (https://doi.org/10.1115/1.4048853)

Introduction

In bioprinting, the bioink contains living cells [2] (including animal, plant, and algae cells). Cells in printed structures are immobilized. Immobilization provides a continuous, sustainable cultivation of plant and algae cells [2]. Therefore, immobilized plant and algae cells can grow faster in their number (higher cell density) and produce more metabolites per cell than cells suspended in liquid [3]. Metabolites derived from plants [2] and algae [4] are used in products manufactured by the pharmaceutical, cosmetic, and food industries. Algae can also produce vanilla flavoring [4], artificial sweetener [5], and antibiotics [6].

It has been reported that increasing extrusion pressure, decreasing needle diameter, or doing both at the same time causes cell viability to decrease in extrusion-based bioprinting with animal cells. After bioprinting, cells are considered viable if they are alive and capable of growth and reproduction [9]. It has also been reported [10] that different cell types exhibit different sensitivities to extrusion pressure and needle diameter during bioprinting.

It is noted that all reported studies regarding effects of extrusion pressure and needle diameter on cell damage in bioprinting used animal cells. For bioprinting using plant or algae cells, there are no reports regarding effects of extrusion pressure or needle diameter on cell viability. Because different cells respond differently to changes in bioprinting conditions (including extrusion pressure and needle diameter) [10], it is unknown how algae cell viability will be affected by changes of extrusion pressure and needle diameter in extrusion-based bioprinting. This study aims to fill this knowledge gap. It reports an experimental study regarding effects of extrusion pressure and needle diameter on cell viability of Chlamydomonas reinhardtii algae in printed samples using an extrusion-based bioprinter.

Materials and Methods

The algae cells were prepared as described in study 1. The procedure described in study 1 was followed to synthesize alginate-methylcellulose bioink.

The samples were designed using Fusion 360 software (Autodesk, USA). Each sample was a disk with diameter of 15 mm and thickness of 1.5 mm. The printing was done using Allevi 2 bioprinter in a similar manner as described in study 1 followed by immersing the printed constructs in 4% w/v $CaCl_2$ solution for crosslinking.

Two sets of one-factor-at-a-time experiments were conducted to investigate the effect of extrusion pressure and the effect of needle diameter on cell viability. For the first set of experiments, samples were printed by varying extrusion pressure. The three levels of extrusion pressure were 3, 5, and 7 bar. Needle diameter was kept constant at 250 μm. For the second set of

experiments, samples were printed by varying needle diameter. The three levels of needle diameter were 200, 250, and 400 µm. Extrusion pressure was kept constant at 4 bar. For both sets of experiments, three samples were printed as replicates at each experimental condition. The constant parameters, 250 µm for needle diameter and 4 bar for pressure, were chosen to achieve a continuous extrusion of strand during printing.

Confocal microscopy, FV1000 microscope (Olympus, Inc., USA), was used in this study to measure cell quantity in printed samples.

Results and Discussion

It was observed that algae cell quantity decreased as extrusion pressure increased. Algae cell quantity was the highest for the samples printed at extrusion pressure of 3 bar, and the lowest for the samples printed at extrusion pressure of 7 bar. These trends were observed in experimental data measured on both day 3 and day 6 post printing. Between day 3 and day 6, the samples printed at 3 bar had the largest increase in algae cell quantity, and the samples printed at 7 bar had the smallest increase in cell quantity. Cells that can grow and reproduce are considered viable [9]. Since only viable cells are capable of multiplying, this trend suggests that the samples printed at 3 bar had the highest number of viable cells, while the samples printed at 7 bar had the lowest number of viable cells.

Algae cell quantity in printed samples increased as needle diameter increased. This trend was observed on both day 3 and day 6 post printing. Between day 3 and day 6, the samples printed with needle diameter of 400 µm had the highest algae cell quantity, and the samples printed with needle diameter of 200 µm had the lowest cell quantity. Because algae cell quantity is an indicator of cell viability, it can be inferred from the data that algae cells in the samples printed with needle diameter of 200 µm and 250 µm were less viable than those in the samples printed with needle diameter of 400 µm.

There are no reported studies on the effects of extrusion pressure or needle diameter on algae cell quantity in printed samples. However, the trends observed from this study are consistent with reported trends about effects of extrusion pressure and needle diameter on cell viability of animal cells in printed samples.

In this study, effects of extrusion pressure and needle diameter on algae cell quantity in printed samples were investigated. Cell quantity was used to determine cell viability. Major findings are as follows:

- Increasing extrusion pressure caused algae cell quantity in printed samples to decrease. This trend was observed on both day 3 and day 6 post printing.
- Increasing needle diameter caused algae cell quantity in printed samples to increase. This trend was observed on both day 3 and day 6 post printing.

VII: Effects of Bioink Viscosity, Extrusion Pressure and Nozzle Diameter in Extrusion Based Bioprinting: Feasible Regions

Note: The results from this study have been published in a journal paper:
Thakare, K., Wei, X.J., Jerpseth, L., Bhardwaj, A., Qin, H.M., and Pei, Z.J., 2020, "Feasible regions of bioink composition, extrusion pressure, and needle size for continuous extrusion-based bioprinting," Journal of Manufacturing Science and Engineering, Vol. 142, No. 12, 124501. (https://doi.org/10.1115/1.4048000)

Introduction

In extrusion-based bioprinting, it is important to understand how process parameters affect the final form of 3D printed constructs [17]. As strand is a basic building block for 3D printed constructs in extrusion-based bioprinting [3], it is vital to know what extrusion pressure to use for a given nozzle diameter when printing with bioink of known viscosity. Currently, there are no such reported studies on bioink of alginate and methylcellulose. This study reveals feasible regions of extrusion pressure and nozzle diameter in extrusion-based bioprinting.

Methods

Aginate:methylcellulose blend was synthesized in the same way as in the study 1. A model of construct consisting of a straight line 5 cm long and 0.1 mm in thickness was designed using Fusion 360 (Autodesk, USA). The printing was done using Allevi 2 bioprinter in a similar manner as described in study 1.

The following parameters were selected for the study:

- Bioink composition: The ratio of alginate and methylcellulose by weight
- Extrusion pressure: The pressure at which bioink is being extruded out of the nozzle
- Nozzle diameter: The nozzle diameter of syringe

Bioink composition was varied by changing methylcellulose content. A wide range of extrusion pressure from 10 psi to 110 psi with increment of 10 psi was chosen. Nozzle diameter determines the resolution of the construct being printed. 5 levels of nozzle diameter were chosen from 23 gauge to 32 gauge.

A treatment refers to each combination of parameter setting. For example, one treatment would comprise of bioink composition of 1:2, extrusion pressure of 50 psi, and nozzle diameter of 27 gauge. Combinations of parameter settings lead to 220 treatments, and 3 replications were made for each treatment.

Results and Discussion

Feasible regions were determined based on extrudability of the bioink, which was classified into following:

- Continuous extrusion: the printed strand was continuous without any breaks
- Intermittent extrusion: the printed strand had breaks and was not continuous
- No extrusion: no strand was printed

If extrudability of the bioink was categorized as “No extrusion” or “Intermittent extrusion”, it was marked outside feasible regions. Only extrudability of the bioink categorized as “Continuous extrusion” was marked in feasible regions. Numerical scores were assigned to the extrudability of bioink; “continuous extrusion” is 3; “intermittent extrusion” is 2; and “no extrusion” is 1.

Highest extrudability is achieved by alginate:methylcellulose ratio of 1 to 1.5 because they have the smallest amount of methylcellulose. Strands are extruded for all nozzle diameters with high pressure of 100 and 110 psi. The strand is properly extruded at all pressure for 23 needle gauge of nozzle diameter except for one intermittent extrusion at pressure of 10 psi.

When methylcellulose content increases, i.e. alginate:methylcellulose ratio of 1 to 2, feasible regions shift toward upper right corner, which is higher pressure and smaller nozzle diameter. On the other hand, regions of ‘No extrusion’ also increase, which is the left bottom corner of lower pressure and larger nozzle diameter.

The feasible regions are further reduced for alginate:methylcellulose ratio of 1 to 2.5. Increased alginate:methylcellulose ratio of 1 to 3 does not further reduced the feasible regions. Instead, the regions of 'Continuous extrusion' slightly increased and 'No extrusion' regions decreased.

In summary, high pressure, small nozzle diameter, and low concentration of methylcellulose can ensure extrudability of bioink in of the extrusion-based bioprinter. However, there are some compromises that we need to be aware. First, high pressure can damage cell viability. Larger nozzle diameter sacrifices print resolution. Lastly, low viscosity affects mechanical strength of printed constructs.

VIII: Effects of Extrusion Temperature and Printing Direction in Bioprinting on Profile Accuracy of 3D Printed Constructs

Note: The results from this study have been published in a conference paper:
Thakare, Ketan, Wei, Xingjian, Qin, Hongmin, and Pei, Zhijian. "Effects of Extrusion Temperature and Printing Direction in Bioprinting on Profile Accuracy of 3D Printed Constructs." Proceedings of the ASME 2019 International Mechanical Engineering Congress and Exposition (IMECE 2019). Volume 3: Biomedical and Biotechnology Engineering. Salt Lake City, Utah, USA. November 11–14, 2019. V003T04A012. ASME. https://doi.org/10.1115/IMECE2019-12150.

Introduction

For extrusion-based printing, dimensional accuracy of 3D printed constructs depends on bioink and printing process parameters. Hydrogels are widely used as bioinks in extrusion-based bioprinting [5] for a couple of reasons. Firstly, hydrogels provide an effective environment for cell growth because of their high-water retention abilities [12]. Secondly, they are viscous in nature, making them extrudable. Various process parameters like extrusion temperature, extrusion pressure, printing speed, and printing direction affect the scaffold profile accuracy. Studies have been reported on effects of printing process parameters using different hydrogels such as alginate-gelatin [13], hyaluronic acid [14], and methylcellulose [9]. However, effects of extrusion temperature and printing direction using Alginate:Methylcellulose hydrogel have not yet been reported. In this experimental study, effects of the extrusion temperature and printing direction on dimensional accuracy (strand thickness) of 3D printed constructs will be determined.

Methods

Four bioink solutions with different ratios of alginate:methylcellulose were made by adding methylcellulose powder (Sigma-Aldrich, USA) to alginate solution in 1:1, 1:1.25, 1:1.5, and 1:1.75 ratio by weight.

Byko-visc Basic EX Viscometer (BYK-Gardener, USA) was used to measure viscositiy of the synthesized bioink solutions. The RPM (rotation per minute) was set according to the viscosity range as recommended in the user manual by manufacturer.

The model of construct was designed using Fusion 360 (Autodesk, USA). The design involved 5 zigzag segments (length of each segment = 0.2 mm) oriented with 90° shift to each other in the horizontal and vertical directions.The printing was done using Allevi 2 bioprinter in a similar manner as described in study 1 followed by immersing the printed constructs in 4% w/v $CaCl_2$ solution for crosslinking. The constructs were then kept at room temperature, under ambient light, and in 100 percent humidity condition for sixty minutes before accuracy measurement.

Dino-Lite AF4915ZT handheld microscope (Dino-Lite, USA) along with DinoCapture software was used to take images and measure strand thickness. Strand thickness was measured at 15 different locations on the construct.

Results and Discussion

Main effect of extrusion temperature

As temperature increases, mean strand thickness increases. It is also evident that the variation in strand thickness has an increasing trend with an increase in temperature. One possible reason for this trend is the effect of increasing temperature on viscosity of hydrogel. Increasing temperature causes the viscosity of hydrogel to decrease. This causes the bioink to spread out once it is extruded, leading to the increase in strand thickness.

The statistical analysis of measurement data using one-way ANOVA resulted in a p-value of <0.001. This implies that temperature has a significant effect on the strand thickness of 3D printed constructs at the significance level of 0.05. The post-hoc analysis using Tukey's test showed that there is a significant difference in the means of strand thickness printed between 35℃ and 40℃ and between 40℃ and 45℃. It means that strand thickness of constructs printed at 35℃ is significantly less than that of constructs printed at 40℃. Also, strand thickness of constructs printed at 40℃ is significantly less as compared to that of constructs printed at 45℃.

Main effect of printing direction

The mean strand thickness is higher for the vertical printing direction than that for the horizontal printing direction. Statistical analysis with one-way ANOVA resulted in a p-value of 0.007. At the significance level of 0.05, direction significantly affects the strand thickness of printed constructs.

Interaction effect of extrusion temperature and printing direction

The p-value of 0.397 shows that the interaction effect of temperature and direction on strand thickness of printed constructs is statistically significant at the significance value of 0.4. At temperature of 35℃, strand thickness does not change much as printing direction changes from horizontal to vertical; at temperature of 40℃, strand thickness increases as printing direction changes from horizontal to vertical; and at temperature of 35℃, strand thickness decreases as printing direction changes from horizontal to vertical.

IX. Experimental Investigation of Alginate-Methylcellulose Composition and Printing Direction on Dimensional Accuracy of 3D Printed Constructs

Note: The results from this study have been published in conference paper:
Thakare, Ketan, Jerpseth, Laura, Qin, Hongmin and Pei, Zhijian. "Experimental investigation of alginate-methylcellulose composition and printing direction on dimensional accuracy of 3d printed constructs." Proceedings of the 15th International Manufacturing Science and Engineering Conference (MSEC 2020). Cincinnati, Ohio, USA. June 22-26, 2020. https://doi.org/10.1115/MSEC2020-8478.

Introduction

3D bioprinting is a biomedical application of additive manufacturing technique [1]. 3D bioprinting (referred to as bioprinting hereafter) involves simultaneous deposition of living cells and biomaterials in a layer by layer fashion to fabricate structures comparable to native tissues [2].

For bioprinted tissues to effectively mimic native tissues, they need to have adequate dimensional accuracy. Among different bioprinting methods, extrusion-based bioprinting is widely used due to its simplicity, ease-of-use, and compatibility with a wide range of biomaterials.

The smallest material unit that can be printed decides the resolution and dimensional accuracy of bioprinted constructs. In the case of extrusion-based bioprinting, strand is the smallest material unit [3]. The strand width is influenced by bioink properties [4] and process parameters. Hydrogels have been widely used as bioink in extrusion-based bioprinting [5]. Alginate based hydrogels are often used for bioprinting due to their good thixotropic property [6]. Methylcellulose (MC) has been used to enhance the viscosity of alginate hydrogel to make it suitable for extrusion [7]. Several studies [8] [9] [3] [10] have been reported where authors have used strand thickness as an accuracy measurement of printed constructs. Currently, there are no reported studies using strand thickness to investigate effects of bioink composition and printing direction on dimensional accuracy of 3D printed constructs using alginate-methylcellulose bioink. This study is on effects of bioink composition (alginate:methylcellulose ratio) and printing direction on dimensional accuracy of 3D printed constructs.

Materials and Methods

The methods are the same as those used in the fourth study.

Results and discussion

Main effect of composition on strand thickness

As viscosity of bioink increases, mean strand thickness decreases. In other words, with an increase in methylcellulose content from 3%w/v to 6%w/v in bioink for same alginate content of 3%w/v, mean strand thickness decreases. The statistical analysis of measurement data using one-way ANOVA resulted in a p-value of <0.0001. This clearly implies that composition has a significant effect on strand thickness of 3D printed construct. The post-hoc analysis using Tukey's test showed that there is a significant difference between means of strand thickness printed with all four synthesized bioinks. The reason for this decreasing strand thickness trend is that, as methylcellulose concentration increases, the viscosity of bioink increases. On printing the constructs, bioink does not spread out and continues to maintain its shape.

Main effect of printing direction on strand thickness

Mean strand thickness is not affected by printing direction. This conclusion is further supported by the statistical analysis using one-way ANOVA. The p-value obtained is 0.99, showing that printing direction does not significantly affect strand thickness.

Interaction effect of composition and printing direction on strand thickness

The p-value of 0.001 shows that the interaction effect of composition and direction on strand thickness of printed constructs is statistically significant at the significance level of 0.05. It can be inferred that when alginate-methylcellulose proportion is 1:1.75, the strand thickness is different for different directions. However, for alginate-methylcellulose bioink proportion of 1:1.5, there is almost no change in strand thickness for different directions.

Summary on bioprinting studies: Bioprinting fabricates structures via layer-by-layer deposition of biomaterials. Bioprinting with plant and algae cells, termed as 'green bioprinting', has many potential applications, including metal removal from contaminated water. In our preliminary study,

hydrogel filters containing algae cells and those without algae cells were printed. They were then used in a custom-build filtration setup for copper removal from test solution. Our second study investigated effects of printing parameters (extrusion pressure and needle diameter) on algae cell viability in printed samples. In our third study, we investigated feasible regions of bioink composition, extrusion pressure, and needle size for extruding continuous strands. Our fourth study was about effects of extrusion temperature and printing direction on dimensional accuracy of 3D printed constructs using alginate:methylcelluolose hydrogel. Our fifth study was about effects of alginate:methylcellulose bioink composition and printing direction on dimensional accuracy of 3D printed constructs. Moving forward, we plan to study how printed green filters can be used to remove other heavy metals from contaminated water, differences in metal removal between various species of algae, and lifespan of printed green filters. We also aim to develop and characterize novel bioinks that have desired properties (including biocompatibility, cell adhesion, extrudability, and low immunogenicity).

X. Colour-sensitive conjugated polymer inkjet-printed pixelated artificial retina model

In recent years, organic electronic materials have been shown to be a promising tool, even transplanted in vivo, for transducing light stimuli to non-functioning retinas. Here we developed a bio-hybrid optoelectronic device consisting of patterned organic polymer semiconductors interfaced with an electrolyte solution in a closed sandwich architecture in order to study the photo-response of photosensitive semiconducting layers or patterns in an environment imitating biological extracellular fluids. We demonstrate an artificial retina model composed of on an array of 42,100 pixels made of three different conjugated polymers via inkjet printing with 110 pixels/mm^2 packing density. Photosensing through three-colour pixelation allows to resolve incoming light spectrally and spatially. The compact colour sensitive optoelectronic device represents an easy-to-handle photosensitive platform for the study of the photo response of artificial retina systems.

Pixelated polymer artificial retina via inkjet printing. Once the biocompatibility and the optoelectronic operation of the devices was demonstrated, we extended the single polymer layer device to a pixelated, colour sensitive, three-polymer-based device towards an artificial retina model. The size of a human adult retina is typically around 22.0 mm in diameter. Photoreceptors are organized in a well-defined mosaic, where rod densities are predominant in the peripheral retinal region while cones in the central part (fovea). Out of all cones, about 64% are L type, 32% M type and only 2% S type. Relative ratio and position of cones varies greatly among different people even with regular vision. Recently the concepts of pixelated visual implants have been exploited and retinal stimulating pixels (~ 100 μm in diameter) have been obtained by spin-coating, sputtering and photolithography techniques. We designed a simplified model to fabricate the pixelated artificial retina system using the resulting anatomical map of the photoreceptors mosaic and placing locally different polymer semiconductors with specific absorbance spectra via printing techniques (Fig. 7a,b). Conjugated polymers have been previously proposed as promising materials for colour detection due to band gap and optical tunability. We firstly identified polymers with absorbance spectra similar to that of human photoreceptors (for human photoreceptors absorbance we referred to Bowmaker and Dartnall studies (Fig. 7c). Regio-regular P3HT polymer and a blend of P3HT with [6,6]-Phenyl C61 butyric acid methyl ester (PC61BM) (P3HT:PCBM) were used, mimicking well the green cone and rods absorbance spectra, respectively. As a third photosensitive polymer we chose Poly(9,9-di-n-octylfluorenyl-2,7-diyl) (PFO), to mimic S-cones.

Its peak is shifted significantly from both those of P3HT and the P3HT:PCBM blend and thus they are all spectrally well distinguishable. Then the biocompatibility was evaluated for the P3HT:PCBM and PFO layers. No significant differences in the proliferation rate expressed as cell doubling time (CTRL = 1.50 ± 0.02 day; P3HT:PCBM = 1.43 ± 0.04 day; PFO = 1.52 ± 0.14 day) and percentages of proliferating cells (T0: CTRL = 51.14 ± 2.06%; P3HT:PCBM = 49.91 ± 3.09%; PFO = 56.27 ± 2.35%; T3: CTRL = 47.58 ± 1.80%; P3HT:PCBM = 47.78 ± 1.70%; PFO = 46.95 ± 2.39%) were observed on the polymer layers compared to control. Cell death analysed at T0 and T3 was very low, with no differences between CTRL, P3HT:PCBM and PFO. These results indicated no toxicity of all the polymer layers analysed. Thus, a pixelated retina system based on M-cones (P3HT), S-cones (PFO) and rods (P3HT:PCBM) was printed, providing a dichromatic inkjet-printed artificial retina model. The three-polymer bio-hybrid printed device mimics the dichromatic vision of most mammals including rodents often used in biomedical studies such as mice that only possess S- and M-cones. Furthermore, it delineates a starting point for a future trichromatic human artificial retina system. Indeed, the device-concept can be easily extended to other polymers. For instance, a possible candidate to mimic human L-cones (maximal absorption at λ = 560 nm) could be Poly[N-9′-heptadecanyl-2,7-carbazole-alt-5,5-(4′,7′-di-2-thienyl-2′,1′,3′-benzothiadiazole)] (PCDTBT) which has an absorbance spectra maximum at 576 nm.

In this study we assembled a simplified model of the anatomical retinal scheme consisting in a concentric ring design where each annulus represents a different retinal photoreceptor region. This simplification made it possible to selectively shadow-mask the different annuli in order to test the spatial and spectral response of our device. The outermost annulus of 360.5 mm^2 corresponds to rods (P3HT:PCBM), whilst the two central annuli correspond to the M-cones (P3HT) of 12.6 mm^2 and the S-cones (PFO) of 7.1 mm^2 areas respectively. Total diameter was 22.0 mm. Inkjet printing was used for selective deposition of the polymers (Fig. 7d) being a powerful technique that offers excellent design flexibility and precise control in material deposition, enabling contactless, mask-free and digital patterning minimising materials usage and waste produced.

Semiconducting polymer inks formulation (molecular weight, concentration, solvents, viscosity and surface tension) and inkjet deposition represented an important part of creating a complete colour-sensitive artificial retina system. High viscosity, nozzle clogging, agglomeration, precipitation, and uncontrollable drying patterns are among the frequently challenges encountered with inkjet printing. PFO, P3HT and P3HT:PCBM were dissolved in a mixture of chlorobenzene (CB) and tetrahydronaphthalene (THN) (1:1) to obtain inkjet-printable polymer inks. The combination of CB:THN—medium/high boiling point solvent mixture—serves two purposes. CB was used to achieve homogeneous film formation owing to excellent solubility of the chosen polymers in CB. THN (b.p. = 270 °C) was used to prevent the nozzles clogging and to provide reliable jetting over time. Inkjet parameters (pulse voltages, cartridge temperature, substrate temperature, drop spacing, waveform) were carefully adjusted in order to obtain stable droplet formation and to achieve rounded-pixels layout. The number of pixels was 42,100, the density of the artificial photoreceptors was ∼11,000 pixels/cm2 and the corresponding spatial resolution was 267 dpi (dots per inch), with pixel diameters of 95 ± 5 μm. Printing technologies enable placement of different materials in the locations of choice. In the future, with higher resolution techniques being developed (i.e. ≤ 10 μm), one could first scan/image an individual retina and then print the pixels spatially where exactly one wants to place them and this can be done for each individual retina (more costly if one uses photolithographic techniques). Secondly, printing techniques enable deposition on uneven or curved surfaces which can be beneficial for artificial retina concepts.

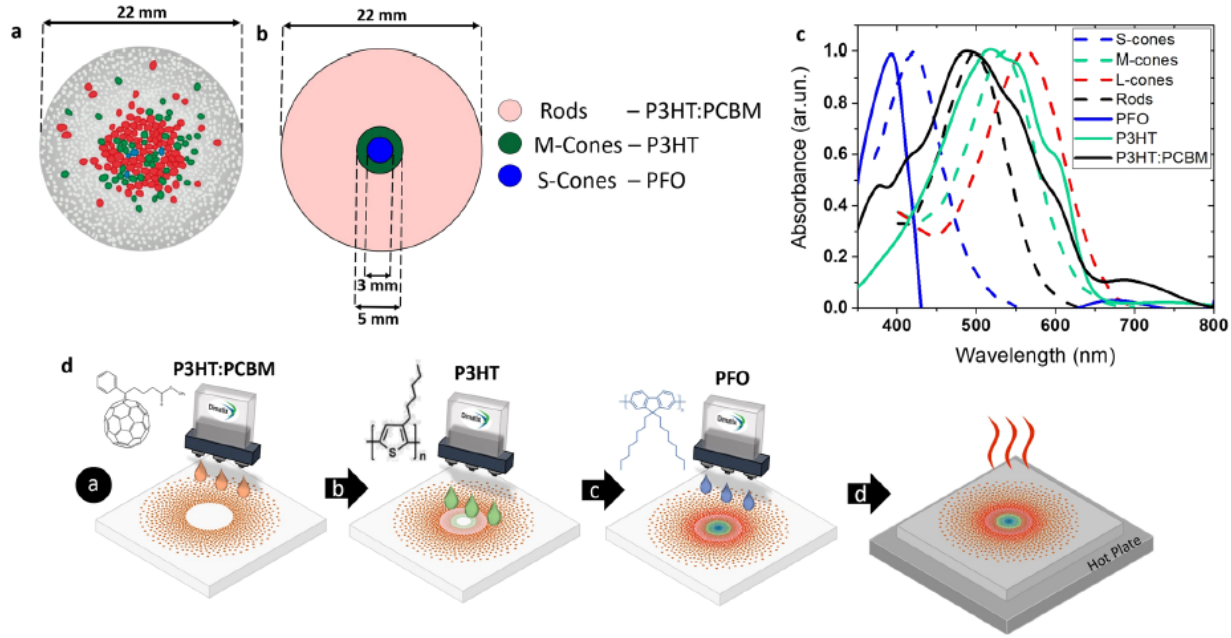

Figure 7. *Model, materials and inkjet printing technique for the fabrication of the pixelated polymer artificial retina system. (**a**) Schematic representation of photoreceptors distributed on a human retina based on anatomical model. The S-Cones (blue), M-Cones (green) and L-Cones (red) are mostly packed into the fovea, while rods (grey) are located mostly in the periphery of the retina. (**b**) A proposed simplified concentrically organized artificial retina model to mimic the spectral response of the M-cones, L-cones and rods from mammalian retina. Concentric geometry model was used for ease of study. Rods-P3HT:PCBM annulus = 360.5 mm2; S-Cones annulus = 7.1 mm2; M-Cones annulus = 12.5 mm2. ((**a**,**b**) images created by using Microsoft PowerPoint). (**c**) Absorbance spectra of human photoreceptors (dashed lines: Rods, S-Cones, M-Cones, L-Cones) compared with those of polymers used in the pixelated inkjet-printed artificial retina of this work (continuous lines). Human photoreceptors absorbance from Bowmaker and Dartnall studies (OriginPro2016 was used). (**d**) Schematics showing the inkjet printing process for the printed artificial retina. Chemical structures of conjugated polymers used for the artificial retina fabrication are shown: step (**a**), PCBM; step (**b**), P3HT; step (**c**), PFO. Step (**d**) represent the thermal annealing.*

Students / Research Faculty involved:
PhD students
Ketan Thakare
Laura Jerpseth
Yuchen Hou
Manuela Ciocca
Research Faculty
Congcong Wu
Kai Wang

Graduated students:
N/A

Publications:

[1] Thakare, K., Jerpseth, L., Pei, Z.J., Tomlin, B., and Qin, H.M., 2021, "3D printing of hydrogel filters containing algae cells for copper removal from contaminated water," accepted to appear in Journal of Manufacturing Science and Engineering.

[2] Thakare, K., Jerpseth, L., Qin, H.M., and Pei, Z.J., 2021, "Bioprinting using algae: effects of extrusion pressure and needle diameter on cell quantity in printed samples," Journal of Manufacturing Science and Engineering, Vol. 143, No. 1, 014501. (https://doi.org/10.1115/1.4048853)

[3] Thakare, K., Wei, X.J., Jerpseth, L., Bhardwaj, A., Qin, H.M., and Pei, Z.J., 2020, "Feasible regions of bioink composition, extrusion pressure, and needle size for continuous extrusion-based bioprinting," Journal of Manufacturing Science and Engineering, Vol. 142, No. 12, 124501. (https://doi.org/10.1115/1.4048000)

[4] M. Ciocca, P. Giannakou, P. Mariani, L. Cinà, A. Di Carlo, M. O. Tas, H. Asari, S. Marcozzi, A. Camaioni, M. Shkunov, T. M. Brown "Colour-sensitive conjugated polymer inkjet-printed pixelated artificial retina model studied via a bio-hybrid photovoltaic device", Scientific Reports, 10, 21457 (2020)

[5] F. Toschi, D. Catone, P. O'Keeffe, A. Paladini, S. Turchini, J. Dagar, T. M. Brown, "Enhanced Charge Separation Efficiency in DNA Templated Polymer Solar Cells" Advanced Functional Materials, 28, 1707126 (2018)

[6] Huachen Cui, Ryan Hensleigh, Desheng Yao, Deepam Maurya, Prashant Kumar, Min Gyu Kang, Shashank Priya, Xiaoyu Rayne Zheng, "Three-dimensional printing of piezoelectric materials with designed anisotropy and directional response", Nature Materials 18, 234 – 241 (2019).

[7] Subhabrata Das, Congcong Wu, Zhaoning Song, Yuchen Hou, Rainer Koch, Ponisseril Somasundaran, Shashank Priya, Bernardo Barbiellini-Amidei, Renugopalakrishnan Venkatesan, "Bacteriorhodopsin Enhances Efficiency of Perovskite Solar Cells", *ACS Appl. Mater. Interfaces* 2019, https://doi.org/10.1021/acsami.9b06372

[8] Yuchen Hou, Kai Wang, Dong Yang, Yuanyuan Jiang, Neela H Yennawar, Ke Wang, Mohan Sanghadasa, Congcong Wu, Shashank Priya, "Enhanced Performance and Stability in DNA-perovskite Heterostructure based Solar Cells", *ACS Energy Lett.*2019, https://doi.org/10.1021/acsenergylett.9b01894

[9] Kai Wang, Yuchen Hou, Bed Poudel, Dong Yang, Yuanyuan Jiang, Min-Gyu Kang, Ke Wang, Congcong Wu, Shashank Priya, "Melanin–Perovskite Composites for Photothermal Conversion", Advanced Energy Materials *9*, 1901753 (2019), https://doi.org/10.1002/aenm.201901753

Conference presentations:

[1] Thakare, Ketan, Jerpseth, Laura, Qin, Hongmin and Pei, Zhijian. "Experimental investigation of effects of needle diameter on algae cell growth in green bioprinting." Proceedings of the 15th International Manufacturing Science and Engineering Conference (MSEC 2020). Cincinnati, Ohio, USA. June 22-26, 2020. https://doi.org/10.1115/MSEC2020-8480.

[2] Thakare, Ketan, Jerpseth, Laura, Qin, Hongmin and Pei, Zhijian. "Experimental investigation of alginate-methylcellulose composition and printing direction on dimensional accuracy of 3d printed constructs." Proceedings of the 15th International Manufacturing Science and Engineering Conference (MSEC 2020). Cincinnati, Ohio, USA. June 22-26, 2020. https://doi.org/10.1115/MSEC2020-8478.

[3] Thakare, Ketan, Jerpseth, Laura, Qin, Hongmin and Pei, Zhijian. “Preliminary investigation of removing copper contamination from water using algae.” Proceedings of the 15th International Manufacturing Science and Engineering Conference (MSEC). Cincinnati, Ohio, USA. June 22-26, 2020. https://doi.org/10.1115/MSEC2020-8521.

[4] Thakare, Ketan, Wei, Xingjian, and Pei, Zhijian. "Dimensional Accuracy in PolyJet Printing: A Literature Review." Proceedings of the 14th International Manufacturing Science and Engineering Conference (MSEC 2019). Volume 1: Additive Manufacturing; Manufacturing Equipment and Systems; Bio and Sustainable Manufacturing. Erie, Pennsylvania, USA. June 10–14, 2019. V001T01A037. ASME. https://doi.org/10.1115/MSEC2019-3018.

[5] Thakare, Ketan, Wei, Xingjian, Qin, Hongmin, and Pei, Zhijian. "Effects of Extrusion Temperature and Printing Direction in Bioprinting on Profile Accuracy of 3D Printed Constructs." Proceedings of the ASME 2019 International Mechanical Engineering Congress and Exposition (IMECE 2019). Volume 3: Biomedical and Biotechnology Engineering. Salt Lake City, Utah, USA. November 11–14, 2019. V003T04A012. ASME. https://doi.org/10.1115/IMECE2019-12150.

[6] Wei, Xingjian, Thakare, Ketan, Zeng, Li, and Pei, Zhijian. "Experimental Investigation of Stratasys J750 PolyJet Printer: Effects of Finish Type and Shore Hardness on Dimensional Accuracy." Proceedings of the ASME International Manufacturing Science and Engineering Conference (MSEC 2019). Volume 2: Processes; Materials. Erie, Pennsylvania, USA. June 10–14, 2019. V002T03A018. ASME. https://doi.org/10.1115/MSEC2019-2999.

[7] Jerpseth, Laura, Thakare, Ketan, Qin, Hongmin and Pei, Zhijian. “Experimental investigation of effects of extrusion pressure on cell growth of bioprinted algae cells in green bioprinting.” Proceedings of the 15th International Manufacturing Science and Engineering Conference (MSEC 2020). Cincinnati, Ohio, USA. June 22-26, 2020. https://doi.org/10.1115/MSEC2020-8481.